

## Combining barotropic and baroclinic simplified models for drift trajectory predictions

Florian Beiser, Håvard Heitlo Holm, Martin Lilleeng Sætra, Nils Melsom Kristensen & Kai Håkon Christensen

**To cite this article:** Florian Beiser, Håvard Heitlo Holm, Martin Lilleeng Sætra, Nils Melsom Kristensen & Kai Håkon Christensen (27 Jun 2024): Combining barotropic and baroclinic simplified models for drift trajectory predictions, Journal of Operational Oceanography, DOI: [10.1080/1755876X.2024.2364975](https://doi.org/10.1080/1755876X.2024.2364975)

**To link to this article:** <https://doi.org/10.1080/1755876X.2024.2364975>



© 2024 The Author(s). Published by Informa UK Limited, trading as Taylor & Francis Group



Published online: 27 Jun 2024.



Submit your article to this journal [↗](#)



Article views: 97








View related articles [↗](#)



View Crossmark data [↗](#)

# Combining barotropic and baroclinic simplified models for drift trajectory predictions

Florian Beiser <sup>a,b</sup>, Håvard Heitlo Holm <sup>a</sup>, Martin Lilleeng Sætra <sup>c,d</sup>, Nils Melsom Kristensen <sup>c</sup> and Kai Håkon Christensen <sup>c,e</sup>

<sup>a</sup>Mathematics and Cybernetics, SINTEF Digital, Oslo, Norway; <sup>b</sup>Department of Mathematical Sciences, NTNU, Trondheim, Norway; <sup>c</sup>Norwegian Meteorological Institute, Oslo, Norway; <sup>d</sup>Department of Computer Science, Oslo Metropolitan University, Oslo, Norway; <sup>e</sup>Department of Geosciences, University of Oslo, Oslo, Norway

## ABSTRACT

The shallow-water equations are often used as a classical simplified ocean model for barotropic ocean dynamics. The same equations can also be used to model simplified baroclinic dynamics through the reduced-gravity model. Herein, we propose to utilise a GPU-accelerated shallow-water simulation framework for representing two decoupled simplified ocean models for each of the barotropic and baroclinic dynamics, and use these models for ensemble prediction of short-term drift trajectories in coastal domains. This system can be used complementary to current operational systems as a lightweight tool for uncertainty quantification and in the future for ensemble-based data assimilation of in-situ observations. We show the relevance of our approach by demonstrating how the barotropic and baroclinic dynamical components are of varying importance at different geographical locations, and that one of the models can be used alone or in combination with the other. We benchmark our approach by showing the resulting ensemble trajectories in reference to deterministic trajectories produced by operational models for three Norwegian coastal regions.

## ARTICLE HISTORY

Received 28 April 2023  
Accepted 19 May 2024

## 1. Introduction

The development of ocean forecasting systems is generally towards increasing spatial resolution. Operational forecasts are typically constrained by the availability of computational resources, meaning the configuration and size of the available compute cluster and the prioritisation among other operational and non-operational compute-intensive jobs. When spatial resolution is of particular importance, for example as in regional models of complex circulation in the coastal zone, resources are often used for a single deterministic ocean forecast with the highest level of detail that fits within the available computational resources and still produces a timely forecast. The result is then a detailed deterministic forecast, but with a lack of uncertainty quantification.

Herein, we describe an ensemble prediction system based on two simplified ocean models that can be considered complementary to fully three-dimensional, primitive equation circulation models (Bleck 2002; Chassignet et al. 2003; Shchepetkin and McWilliams 2005; Madec and the NEMO team 2008). In this

context, ‘simplified’ means that we do not attempt to produce the most realistic representation of the ocean dynamics, but rather develop lightweight models that complement the resource-demanding fully three-dimensional models. The aim is to provide short-term ensemble forecasts of the upper ocean circulation for decision support (Christensen et al. 2018). Since we only seek some predictive ability on short timescales (typically a few hours), we do not seek to model any changes in hydrography due to air-sea interactions, river runoff, or turbulent mixing, but limit ourselves to the classical problem of wave propagation, solving a set of hyperbolic equations for (i) the depth-averaged current (barotropic mode), and (ii) the upper mixed layer (lowest order baroclinic mode). It should be noted that we decouple these modes by assuming a 1.5-layer/reduced-gravity model for the upper ocean. As discussed further below, a coupled two-layer approach is certainly feasible, but our interest here is in the most lightweight system that is still fit for the purpose, exploiting the benefits of having decoupled baroclinic and barotropic modes. The

**CONTACT** Florian Beiser  florian.beiser@sintef.no  Forskningsveien 1, 0373 Oslo, Norway

© 2024 The Author(s). Published by Informa UK Limited, trading as Taylor & Francis Group

This is an Open Access article distributed under the terms of the Creative Commons Attribution License (<http://creativecommons.org/licenses/by/4.0/>), which permits unrestricted use, distribution, and reproduction in any medium, provided the original work is properly cited. The terms on which this article has been published allow the posting of the Accepted Manuscript in a repository by the author(s) or with their consent.

most important coupling effects, which we lose here, would be from advective processes. Other elements of the upper ocean dynamics relevant to oceanic drift, i.e. the wind drag and wind- and wave-induced currents, are parameterised in an accompanying online trajectory model.

The objective of our approach is thus fast on-demand simulations in limited areas, potentially with complex topography; better representation of uncertainty employing large model ensembles; and, further down the line, enabling nonlinear assimilation of in-situ observations from, e.g. drifting buoys (Holm, Sætra, and Brodtkorb 2020; Holm, Sætra, and van Leeuwen 2020). The framework we have developed runs almost exclusively on graphics processing units (GPUs), further speeding up simulations while reducing watts per flops (see, e.g. Huang et al. 2009; Dong et al. 2014). Our interest is in drift trajectory forecasting, which is a crucial component in coastal preparedness and emergency management. Applications range from search-and-rescue operations, planning and organising clean-up of spilled pollutants, to decision support for large drifting objects such as abandoned ships or icebergs. In this context, we are interested in predicting the ocean currents to forecast probabilistic trajectories, with a requirement to do so within tight time frames.

In our previous work, we have presented a GPU-accelerated simulation framework for running shallow-water ocean models (Røed 2019) on realistic domains (Brodtkorb and Holm 2021). We refer to this framework as ‘GPU Ocean’. The motivation has been to explore heterogeneous computing for storm-surge modelling (Kristensen et al. 2022), and we have also been using it for probabilistic forecasting of drift trajectories using various methods for data assimilation (Holm, Sætra, and Brodtkorb 2020; Holm, Sætra, and van Leeuwen 2020; Beiser et al. 2023). We have used high-resolution finite volume schemes, and a significant effort has been made to make these schemes well balanced for geophysical (rotational) flows and applicable for realistic topography, while optimising the code for fast simulations. A weakness of this approach, however, is that we neglect the baroclinic dynamics driven by spatial differences in salinity and temperature, which is an important contribution to particle drift (Röhrs and Christensen 2015).

In this work, we combine the barotropic simplified ocean model from Brodtkorb and Holm (2021) with a reduced-gravity model for the upper mixed layer of the ocean. We use the same GPU-accelerated computational framework for both models and initialise and force our simulations using available deterministic forecasts made from traditional coastal ocean forecasting

system. Depending on the local conditions, in some cases only the contribution of only one of the simplified models may be relevant, and in other cases both models may be needed. Then, we compute drift trajectories assuming the drift is a sum of the baroclinic and barotropic currents. While perturbing various input parameters for the trajectory modelling, such as wind strength and direction, we facilitate the construction of large drift trajectory ensembles through the cross products between smaller barotropic and larger baroclinic ensembles.

*Related work:* Reduced-gravity models were developed early on for modelling of the mixed layer dynamics, cf. Gent and Cane (1989), Arango and Reid (1991), Kim and Yoon (1996), and Dellar and Salmon (2005) also used the shallow-water equations to do so. Reduced-gravity models can also be useful for other applications, e.g. Samelson et al. (2019) use a one-layer, reduced-gravity, quasigeostrophic model to simulate open-ocean mesoscale variability; and Wang et al. (2003) employ a two-layer, reduced-gravity model to simulate dense water flow on continental shelves.

An alternative to our proposed combination of decoupled baroclinic and barotropic shallow-water models, is to use the coupled two-layer shallow-water equations as the simplified ocean model. The two-layer model assumes vertical stratification of the ocean, with two shallow-water layers interacting by the dynamic depth of their intersection (see, e.g. Røed 2012 for derivation), and accounts for baroclinic and barotropic physics. Although apparently well-suited for our application and proved to be suited for GPU-acceleration (de la Asunción et al. 2016), numerical implementation of the two-layer model is more challenging due to non-conservative terms and possible loss of hyperbolicity (Castro-Díaz et al. 2011). Here, we reuse existing code for the barotropic simulator, hence a limited amount of work is needed to extend existing one-layer shallow-water codes. Having two separate models is also more flexible, making it possible to turn on and off modes depending on the case and domain. Furthermore, we are able to span an ensemble by combining different pairs of barotropic and baroclinic realizations.

In the work by Kudryavtsev et al. (2019), a simplified ocean model is built under the distinct consideration of barotropic and baroclinic modes for the application of tropical cyclones – for this special scenario, they find analytical solutions under the assumption of a non-changing mixed-layer depth. Peña-Molino et al. (2014) treat barotropic and baroclinic mass transport across the Antarctic Circumpolar current separately, as they are, on average, in opposite directions, and they find that barotropic and baroclinic transport is spatially variable.

Herein, we rely on an online built-in trajectory model (see Section 2.3), with the OpenDrift (Dagestad et al. 2018) trajectory framework used as a reference. The OpenDrift package is a part of the emergency preparedness at the Norwegian Meteorological Institute, and has internal models for oil spills, disabled ships drift forecasting, search and rescue operations, and iceberg monitoring. It uses 3D fields of the ocean state to make an offline trajectory forecast. For a thorough survey of drift in the ocean and trajectory modelling we refer the reader to van Sebille et al. (2020) and Röhrs et al. (2023), and references therein.

*Outline.* The article is structured as follows: Section 2 describes how the shallow-water equations are used for both the barotropic and the baroclinic parts of the simplified ocean model. Numerical results for idealised conditions to show the validity of the reduced-gravity model are presented in Section 3. Section 4 showcases the application of the purely barotropic, purely baroclinic, and combined barotropic-baroclinic models for drift trajectory forecasting in ensemble prediction systems (EPSs) for three different Norwegian coastal areas. The paper ends with a discussion in Section 5.

## 2. Simplified ocean models for barotropic and baroclinic motion

In the following, we describe the barotropic and baroclinic versions of our simplified ocean model, and how we combine the currents from the two independent models for drift trajectory modelling. A complete derivation of the barotropic model can be found in Røed (2019), whereas the computational simulation framework used herein is presented in detail in Brodtkorb and Holm (2021). We will nevertheless give a brief overview of the barotropic model for completeness and to emphasise its similarities and differences from the baroclinic model. Since we will show that the two models can be represented by the same mathematics, we will use  $\tilde{\cdot}$  and  $\bar{\cdot}$  to represent variables belonging to the barotropic and the baroclinic models, respectively, when the same symbols are needed. To improve readability, we will also abuse this notation so that, e.g.  $\tilde{h}u$  represents  $\tilde{h}\tilde{u}$ .

### 2.1. Barotropic model

The shallow-water equations are a well-established barotropic ocean model, which can be derived under simplifying assumptions from the primitive equations. The equations form a hyperbolic conservation law, conserving mass and momentum within a

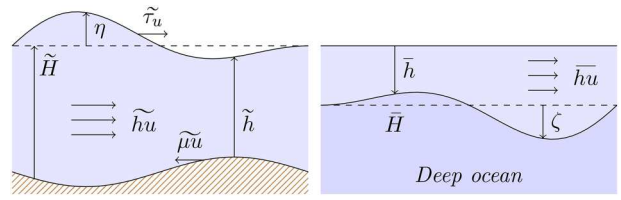


**Figure 1.** Overview of variables used in the shallow-water models, here shown in one dimension. To the left, we see the barotropic model covering the entire water column, and to the right we see the baroclinic model capturing the dynamics within the mixed layer.

rotating frame of reference. They model depth-averaged horizontal velocities and thereby neglect the vertical component of the momentum. This results in a single-layer two-dimensional model, that can be written as

$$\begin{aligned} & \begin{bmatrix} \eta \\ \tilde{h}u \\ \tilde{h}v \end{bmatrix}_t + \begin{bmatrix} \tilde{h}u \\ \tilde{h}u^2 + \frac{1}{2}g\tilde{h}^2 \\ \tilde{h}uv \end{bmatrix}_x + \begin{bmatrix} \tilde{h}v \\ \tilde{h}uv \\ \tilde{h}v^2 + \frac{1}{2}g\tilde{h}^2 \end{bmatrix}_y \\ &= \begin{bmatrix} 0 \\ f\tilde{h}v \\ -f\tilde{h}u \end{bmatrix} + \begin{bmatrix} 0 \\ g\tilde{h}\tilde{H}_x \\ g\tilde{h}\tilde{H}_y \end{bmatrix} + \begin{bmatrix} 0 \\ \tilde{\tau}_u \\ \tilde{\tau}_v \end{bmatrix} + \begin{bmatrix} 0 \\ -\tilde{r}u\sqrt{\tilde{u}^2 + \tilde{v}^2} \\ -\tilde{r}v\sqrt{\tilde{u}^2 + \tilde{v}^2} \end{bmatrix}. \end{aligned} \quad (1)$$

Here, and as shown in Figure 1,  $\eta$  is the sea-surface deviation from mean equilibrium level and  $\tilde{H}$  is the static equilibrium depth, meaning that  $\tilde{h} = \tilde{H} + \eta$  is the total water depth. The momentum is then denoted by  $\tilde{h}u$  and  $\tilde{h}v$  along the  $x$ - and  $y$ -axis, respectively, and subscripts  $t$ ,  $x$  and  $y$  are used for temporal and spatial derivatives. Furthermore,  $g$  is the gravitational constant,  $f$  is the Coriolis parameter accounting for the rotating frame of reference, and  $\tilde{\tau} = [\tilde{\tau}_u, \tilde{\tau}_v]$  is the wind stress calculated as in Large and Pond (1981). The final source term accounts for bed friction and is modelled by a parameterised nonlinear function inspired by the Manning formula (see Dyakonova and Khoperskov (2018)), with dimensionless parameter  $\tilde{r}$ .

$$\tilde{\mu} = -r \frac{\sqrt{\tilde{u}^2 + \tilde{v}^2}}{\tilde{h}} \quad (2)$$

To simulate (1), we use the GPU-accelerated simulation framework presented in Brodtkorb and Holm (2021). The framework is designed to run barotropic simulations on realistic domains and can be initialised by operational 3D ocean forecasts<sup>1</sup> and optionally forced by weather forecast parameters such as wind

and atmospheric pressure. It can run with both higher and lower resolution than what has been used operationally, and supports nested simulations where the operational forecast is used as boundary conditions. The computational grid is assumed to be uniform with grid cells of size  $(\Delta x, \Delta y)$ , but can have arbitrary orientation, meaning that the Coriolis parameter  $f$  varies along the direction towards north, and not along the  $y$ -axis as is often the case.

Within the framework, we solve (1) numerically by a slightly modified version of the well-balanced high-resolution finite volume scheme proposed by Chertock et al. (2018). The scheme is designed to be well-balanced with respect to special cases of geostrophic balance, and is of second order. We solve the equations with an explicit second-order strong stability-preserving Runge-Kutta scheme (Gottlieb and Shu 1998), with time step lengths restricted by the CFL-condition,

$$\Delta \tilde{t} \leq \frac{1}{4} \min \left\{ \frac{\Delta x}{\max |\tilde{u} \pm \sqrt{g\tilde{h}}|}, \frac{\Delta y}{\max |\tilde{v} \pm \sqrt{g\tilde{h}}|} \right\}. \quad (3)$$

GPUs are designed based on the single-instruction multiple-data (SIMD) paradigm (Sanders and Kandrot 2010; NVIDIA 2023), in which a large set of computational cores carry out the same set of mathematical operations on different data. Explicit numerical schemes for solving partial differential equations, such as the one we use to solve (1), are particularly well-suited for implementation on such hardware, as these schemes can be said to be *embarrassingly parallel*. This means that each updated discrete variable can be found independently from all other updated variables, which allows for all of the variables to be updated completely in parallel. This is in contrast to implicit methods, where each updated variable also depends on the values of other updated variables. For early examples of GPU-accelerated shallow-water simulations, see de la Asunción et al. (2011) and Brodtkorb et al. (2012).

## 2.2. Baroclinic model

The ocean is often stratified with a well defined pycnocline. It separates the upper layer, which is typically a  $O(10 \text{ m} - 100 \text{ m})$  thick layer of well-mixed water with density  $\rho_1$ , from the deep lower layer with density  $\rho_2$ . The upper mixed layer is directly influenced by winds and breaking waves, while the ocean interior is more weakly coupled to the atmospheric forcing. The mixed-layer depth (MLD) is neither static nor spatially uniform, and the spatial gradients in the mixed layer are central to the upper ocean dynamics.

To derive the baroclinic shallow-water model (see Appendix 1), we use a two-layer model as a starting point (e.g. Røed 2012). We employ the rigid-lid approach ( $\eta = 0$ ) for the surface elevation and decouple the upper layer from the lower layer by assuming that the latter is infinitely deep. Then, we obtain the so-called 1.5-layer model for the upper ocean:

$$\begin{aligned} & \begin{bmatrix} \zeta \\ \bar{h}\bar{u} \\ \bar{h}\bar{v} \end{bmatrix}_t + \begin{bmatrix} \bar{h}\bar{u} \\ \bar{h}\bar{u}^2 + \frac{1}{2}g'\bar{h}^2 \\ \bar{h}\bar{u}\bar{v} \end{bmatrix}_x + \begin{bmatrix} \bar{h}\bar{v} \\ \bar{h}\bar{u}\bar{v} \\ \bar{h}\bar{v}^2 + \frac{1}{2}g'\bar{h}^2 \end{bmatrix}_y \\ &= \begin{bmatrix} 0 \\ f\bar{h}\bar{v} \\ -f\bar{h}\bar{u} \end{bmatrix} + \begin{bmatrix} 0 \\ \bar{\tau}_u \\ \bar{\tau}_v \end{bmatrix} + \begin{bmatrix} 0 \\ -\bar{r}\bar{u}\sqrt{\bar{u}^2 + \bar{v}^2} \\ -\bar{r}\bar{v}\sqrt{\bar{u}^2 + \bar{v}^2} \end{bmatrix}. \end{aligned} \quad (4)$$

Here, and as shown in Figure 1,  $\bar{h}$  is the MLD, given as  $\bar{h} = \bar{H} + \zeta$ , where  $\zeta$  is positive downwards and the deviation from equilibrium MLD  $\bar{H}$ . Furthermore,  $\bar{\tau} = [\bar{\tau}_u, \bar{\tau}_v]$  is the wind forcing, and  $\bar{r}$  is the friction coefficient between the two layers. Most importantly,  $g'$  is the reduced gravity, given by

$$g' = \frac{\rho_2 - \rho_1}{\rho_2} g. \quad (5)$$

Note that (4) is also called reduced-gravity model and has the same mathematical structure as the shallow-water model in (1), with the only difference being the physical meaning of the deviation from equilibrium depth ( $\zeta$  vs.  $\eta$ ) and the gravitational constant ( $g'$  vs.  $g$ ). This means that the GPU-accelerated simulation framework (Brodtkorb and Holm 2021) can be used directly to simulate baroclinic dynamics, as well as barotropic. A consequence of the reduced gravity and the relatively small values of  $\bar{h}$ , is that the CFL-conditions in (3) allows us to take larger time steps. Whereas the barotropic model needs to take time steps in the order of 1 s, the baroclinic model can run with time steps in the order of 1 min to 2 min, which results in significantly faster baroclinic simulations than barotropic simulations of the same grid and time range. Therefore, we can add the baroclinic mode very inexpensively (with regards to computational resources).

A drawback of our approach is that we obviously lose important elements of the dynamics that stem from the coupling between the barotropic and baroclinic modes. Perhaps most important in the context of short-term simulations is that the baroclinic mode phase speeds in our reduced-gravity model are only functions of the reduced gravity and the mixed layer depth, while in reality the phase speeds depend on the thicknesses of both layers, with increasing error as the lower layer becomes shallower, such as is often the case in the coastal zone.

This issue can at least partially be addressed by perturbing the MLD and the reduced gravity separately, and we will show some examples of this approach in Section 4.

### 2.3. Trajectory model

To predict drift trajectories, we combine independent simulations of the barotropic and baroclinic models. A drifter is then primarily advected by the simulated currents  $[\tilde{u}, \tilde{v}]$  and  $[\bar{u}, \bar{v}]$ , together with a contribution from the wind  $[u_w, v_w]$ . The direct contribution from the wind (the windage) depends largely on the shape of the drifting object. In this work, we are mainly interested in objects that are mostly submerged, so that their drift trajectories primarily depend on the currents and only to a limited extent on the wind. We model windage through a leeway coefficient  $\psi$  that is an object dependent fraction of the wind speed. Hence, a drifter with position  $(x_t, y_t)$  will be advected according to

$$\begin{aligned} x_{t+\Delta t} &= x_t + \Delta t(\tilde{u}(x_t, y_t, t) + \bar{u}(x_t, y_t, t) + \psi u_w(x_t, y_t, t)), \\ y_{t+\Delta t} &= y_t + \Delta t(\tilde{v}(x_t, y_t, t) + \bar{v}(x_t, y_t, t) + \psi v_w(x_t, y_t, t)). \end{aligned} \quad (6)$$

We model the trajectories integrated in the GPU-framework to avoid copying data from the GPU, which would have been a major bottleneck for performance. Furthermore, we also avoid large amounts of output files that would be needed as input for a separate offline trajectory model. In practice, due to the large differences in time-step sizes between the two models, we need to take many steps with the barotropic model for each time we evolve the baroclinic model. We advect the drifters with the same time step and frequency as the barotropic model while using the most recent baroclinic time step, as shown in Algorithm 1. Note that when looking up values for the currents  $u$  and  $v$ , we interpolate in space, but not in time. This is because the information from the previous time step is lost after we update the model with the second-order Runge-Kutta step.

### 2.4. Model perturbations

We now look at ways to perturb initial conditions and external forcings from deterministic operational ocean forecasts. In our demonstration cases, the data is produced by ROMS-based 3D models, containing hourly time series of 3D currents, temperature, salinity, and sea-level, in addition to surface winds from the numerical weather model that forces the 3D ocean models.

**Algorithm 1** Simulation of drift trajectories using a combination of the barotropic and baroclinic models.

---

```

 $\tilde{t}, \bar{t} \leftarrow 0$ 
Initialize drifter:  $(x, y) \leftarrow (x_0, y_0)$ 
while  $\tilde{t}, \bar{t} < t_{\text{end}}$  do
    Evolve baroclinic simulator  $\bar{t} \leftarrow \bar{t} + \Delta \bar{t}$ 
    while  $\tilde{t} < \bar{t}$  do
        Evolve barotropic simulator  $\tilde{t} \leftarrow \tilde{t} + \Delta \tilde{t}$ 
        Advect drifter:
         $x \leftarrow x + \Delta \tilde{t}(\tilde{u}(x, y, \tilde{t}) + \bar{u}(x, y, \bar{t}) + \psi u_w(x, y, \tilde{t}))$ 
         $y \leftarrow y + \Delta \tilde{t}(\tilde{v}(x, y, \tilde{t}) + \bar{v}(x, y, \bar{t}) + \psi v_w(x, y, \tilde{t}))$ 
    end while
end while
    
```

---

*Barotropic initial and boundary conditions:* For relatively small domains, such as those considered in this paper, the barotropic signals are mainly driven by the boundary conditions, and a common source of error in coastal areas is tidal phase. We therefore introduce perturbations in the barotropic models by timeshifting the initial and boundary conditions. Furthermore, drift trajectories can be sensitive to the location of eddies, and by timeshifting initial conditions we also get slight perturbations on the placements of eddies within the domain.

*Mixed-layer depth and reduced gravity:* The MLD can be defined in many different ways (e.g. Brainerd and Gregg 1995; de Boyer Montégut et al. 2004; Giunta and Ward 2022) and in our examples we choose a density criterion, where we compute the potential densities from temperature and salinity (Fofonoff and Millard 1983) read from the 3D operational model. We then choose an initial MLD based on an isopycnal surface with a vertical position that we deem to be overall most representative of the pycnocline in our model domain. In some grid cells, the MLD may not be well-defined. We extrapolate from the closest ‘valid’ grid cells in such cases. The variations in the value of the density criterion is used to perturb the baroclinic model ensemble. As already mentioned, we expect errors in the phase speed of the baroclinic modes, hence we use the possibility to perturb the reduced gravity  $g'$  independently from the MLD perturbations.

*Wind field:* In this work, we obtain hourly deterministic wind fields from the operational ocean models. We then perturb the wind influence onto the models by rotating the entire wind field by some angle. A more realistic way to obtain uncertain wind fields would be to use the ensemble of wind fields from a probabilistic atmospheric forecasts, if available.

*Wind stress:* We calculate the wind stress  $\tilde{\tau}$  using the approach from Large and Pond (1981), which we apply directly to the depth-averaged currents in the barotropic model. However, upper ocean layers have a more direct response to wind forcing than depth-averaged currents. In particular with thin mixed layers, we expect that large momentum fluxes from the atmosphere are partially

communicated instantaneously further down to the deep ocean through the shear stress between the layers. This could be obtained by locally increasing the inter-layer friction coefficient, but to increase the freedom of the reduced-gravity model, we instead fix a friction coefficient  $\bar{\tau}$  for the entire domain and reduce the wind stress  $\bar{\tau} = \tau_0 \tilde{\tau}$  by an uncertain factor  $\tau_0 \leq 1$ .

*Frictional forces at the base of the MLD:* The friction in the reduced-gravity model represents the flux of momentum between the mixed layer and the ocean interior from shear stresses, near-inertial waves, and so on. As just mentioned, this is another way to reduce momentum in the upper layer, where frictional forces however depend on an acceleration of the water column. It may feel redundant but having both parametrizations gives more flexibility in the modelling. We do not consider any details of these mechanisms here and simply consider them parametrised within the uncertain friction coefficient  $\bar{\tau}$ .

*Numerical drifters:* In a realistic case of trajectory modelling in support of, e.g. search-and-rescue operations, the initial position is likely to be a major source of uncertainty. Since our aim here is to explore the uncertainties associated with the modelling systems, we do not perturb initial positions of our numerical drifters in our examples. We perturb the windage, through the leeway coefficient, to compensate for unresolved near-surface vertical shear in the currents, using distributions with high probability for  $\psi \in [0.01, 0.05]$  (e.g. Sutherland et al. 2020), which is randomly assigned to each numerical drifter.

### 2.5. Combined drifter ensembles

Since the two simplified ocean models from Sections 2.1 and 2.2 are not coupled, we can run multiple barotropic and baroclinic simulations independently. A cross product of barotropic and baroclinic simulations spans out a large set of ocean currents that can be used for trajectory modelling. In principle, if we have an ensemble of  $N_{bt}$  barotropic models and an ensemble of  $N_{bc}$  baroclinic models, we can combine any pair of realizations from each of the ensembles to obtain  $N_{bt} \times N_{bc}$  combined ocean states. Since we model passive drifters that do not influence the ocean state, we can also advect drifters with different leeway coefficients within each combined ensemble member. With  $N_\psi$  different leeway coefficients, we forecast the location of drifting objects based on  $N_{bt} \times N_{bc} \times N_\psi$  simulated drift trajectories.

### 2.6. Initialization from 3D operational models

In all numerical experiments presented in this paper, we assume that we have a hourly results from a

deterministic 3D ROMS model. For simplicity, we initialise and run our simplified models using the same horizontal grid resolution as the 3D model, meaning that landmask and bathymetry data is directly available.

The barotropic models is straightforward to initialise. Most often,  $\eta$ ,  $\bar{H}$ ,  $\tilde{u}$  and  $\tilde{v}$  are available directly from the 3D simulation results and can be used directly. However, if  $\tilde{u}$  and  $\tilde{v}$  are not available, it is a simple procedure to obtain  $\bar{h}u$  and  $\bar{h}v$  by numerical integration of  $u$  and  $v$ , respectively, through the water column in every horizontal grid cell.

For the reduced-gravity models, we define  $\bar{H} \equiv 0$  and initialise  $\zeta$  according to the isopycnal obtained from a suitable MLD criterion. We then approximate the baroclinic currents by subtracting the barotropic current and integrating vertically, as

$$\bar{h}u = \int_{-\zeta}^0 u - \tilde{u} dz \quad \text{and} \quad \bar{h}v = \int_{-\zeta}^0 v - \tilde{v} dz, \quad (7)$$

for each grid cell in the domain. To compute the reduced gravitational constant from (5), we first compute the potential densities<sup>2</sup> for each point in the 3D grid. Then, we let  $\rho_1$  and  $\rho_2$  be the mean volumetric averages of the potential energies above and under the MLD, respectively.

## 3. Assessing the baroclinic model

The barotropic part of the model from Section 2.1 is described in Holm, Brodtkorb et al. (2020) and Brodtkorb and Holm (2021). Here we focus on evaluating the baroclinic model from Section 2.2. Coastal waves may have a significant influence on the dynamics in fjords through influencing the exchanges with the open ocean, and in some large fjord systems the spatial scales may allow for rotational effects on the internal wave dynamics. An idealised Kelvin wave test case is therefore provided in Appendix 2. Here, we apply the reduced-gravity model to a high-resolution scenario in the inner Oslofjord, and compare our simulation results against a survey of tidally induced baroclinic currents (Staalstrøm et al. 2012), and assess the model's applicability through drift trajectories, short-term prediction, and computational performance.

### 3.1. Tidally induced baroclinic currents in the inner Oslofjord

The inner and outer parts of the Oslofjord are separated by a shallow and narrow sill outside of the small city of Drøbak (see Figure A3(b)). There are no significant freshwater sources in the inner Oslofjord, and the currents in the inner fjord are mainly driven by tidally induced baroclinic waves generated at the sill in the southern end,

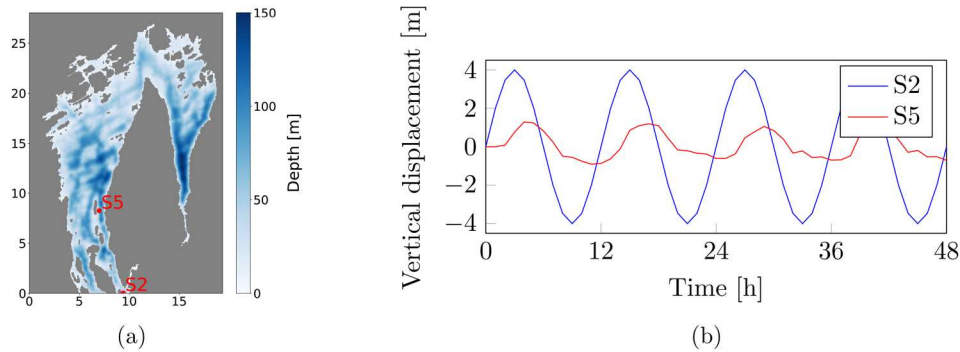


**Figure 2.** The inner Oslofjord with selected observation locations from Staalstrøm et al. (2012) marked by red dots and the simulated vertical displacement in these locations. (a) Bathymetry of inner Oslofjord with locations ‘S2’ and ‘S5’, and axes in km and (b) Vertical displacement of  $\zeta$  at locations ‘S2’ and ‘S5’. Note that S2 essentially describes the set boundary conditions.

and the wind forcing. In the following, we will focus on the tidal forcing. We consider a  $50\text{ m} \times 50\text{ m}$  uniform grid covering the inner Oslofjord, made from re-projecting data from the operational FjordOs model (Hjelmervik and Kristensen 2019). The resulting  $387 \times 561$  grid encompasses a bit less than a  $20\text{ km} \times 30\text{ km}$  domain, as it can be seen for the bathymetry in Figure 2(a).

Staalstrøm et al. (2012) presented a survey of the tide-induced upper layer dynamics in the inner Oslofjord during spring time. We use these results as reference to assess our reduced-gravity model. They refer to observation locations called ‘S2’ just after the sill, where our computational domain starts, and ‘S5’ about 7 km further into the fjord. Both locations are marked in Figure 2(a). We model the boundary conditions to correspond to the observations made at location S2, and use a constant mixed-layer depth of 15 m for initial conditions (cf. Staalstrøm et al. 2012, Table 2). For the boundary conditions, we use the flow-relaxation scheme (Davies 1976) at the sill, where an island separates the sill into a right and left branch. As external solutions, we employ a sine-shaped  $\bar{v}$ -current with amplitude 0.3 m/s and a  $\zeta$ -displacement with amplitude 4 m in the right branch. The values for the amplitudes are found in Staalstrøm et al. (2012, Figure 6b, 8a) and both waves have a period of 12 h. In the left branch,  $\bar{v}$  is not forced from the boundary. The boundary conditions for  $\bar{u}$  are kept zero everywhere. Moreover, Staalstrøm et al. (2012, Table 2) suggests a density difference of around  $10\text{ kg/m}^3$ , leading to a reduced gravity  $g' = 0.1\text{ m/s}^2$ . The friction coefficient is finally set to 0.0015 m and the simulation is run without wind forcing for a time span of two days. Our model results then produce signals with phase speeds of about 1.2 m/s, which is in good agreement with Staalstrøm et al. (2012, Section 3.1), and corresponding to a Rossby radius of a bit more than 10 km. Figure 2(b) shows the results of the reduced-

gravity model, along with the boundary conditions in S2. The values for  $\zeta$  at S5 have a significant reduced amplitude with maximum values at about 1 m, corresponding to about 25% of the amplitude at S5. The signal also lags in time. This is again in accordance with the observations in Staalstrøm et al. (2012, Section 3.2).

### 3.2. Baroclinic contributions to drift trajectories

To evaluate the roles of the baroclinic and barotropic modes, we also run the barotropic model with idealised conditions. Again, we initialise all variables to zero, and force with tidal signals of up to 0.1 m/s current speed and 0.15 m displacement, in accordance to typical values from FjordOs. We demonstrate the application of Algorithm 1 for a 48 h simulation.

Figure 3 shows the resulting drift trajectories for a set of six drifters, where the initial drifter positions are annotated with letters, (a) shows trajectories using only the barotropic currents, and (b) shows trajectories using the combined currents as described in Section 2.3. The crosses mark the final drifter positions. We note that the drifters seeded in the barotropic model barely move at all. In contrast, drifters using combined current information travel longer distances. For them, the main contribution to the drift comes from the baroclinic model. Some drifters are mostly advected back and forth by the tidally induced currents, while other trajectories are more irregular or persistent in certain directions.

Our baroclinic model and method of initialisation are simple, and to illustrate some of the challenges associated with capturing the non-barotropic flows, we initialise two baroclinic model fields from the operational hindcast produced by the FjordOs model using data separated by one hour. We then run the simulation initialised by the earliest point in time for one hour to catch up with the other, and compare these currents. Figure 4 shows the results. Here, we have used MLD



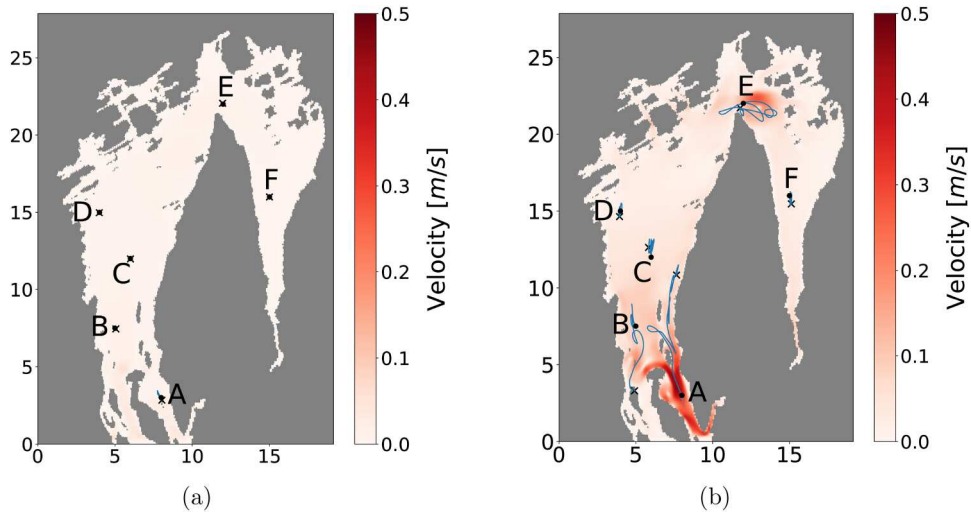


**Figure 3.** Drift trajectories for different simplified models under idealised conditions. The background shows particle velocity after 48 h, and the axes are in km. (a) Barotropic drift trajectories and (b) Trajectories for combined currents.

criterion  $\rho = 1023 \text{ kg/m}^3$  and no friction. The main dynamical features are reproduced in our reduced-gravity model, e.g. the jet entering the fjord from the sill at the southern boundary, the eddy in the widest section of the fjord, and the current bending around the headland in the northern part of the domain. The initial state contains imbalances, however, leading to some of the energy being lost to noise, and it is evident that the overall strength of the flow is reduced.

### 3.3. Computational performance

A comparison of the wall run times provides us with estimates of how many ensemble members we can

afford to run for the same computational costs as a full 3D simulation. For the idealised barotropic and baroclinic simulations, the computational cost is assessed as the wall time which the numerical scheme requires to simulate one hour on a NVIDIA GeForce RTX 3090 using 0.8 as Courant number. Instead of comparing directly to FjordOS, which covers in its full extent a larger domain with a curvi-linear grid, we consider two independent idealised ROMS setups with the same spatial extent as the GPU models. One of the ROMS setups was run in full 3D mode (including both barotropic and baroclinic physics) with ten vertical layers, denoted as *Full 3D*, and one in 2D mode (only utilising the barotropic physics of ROMS), denoted as *Barotropic 2D*.

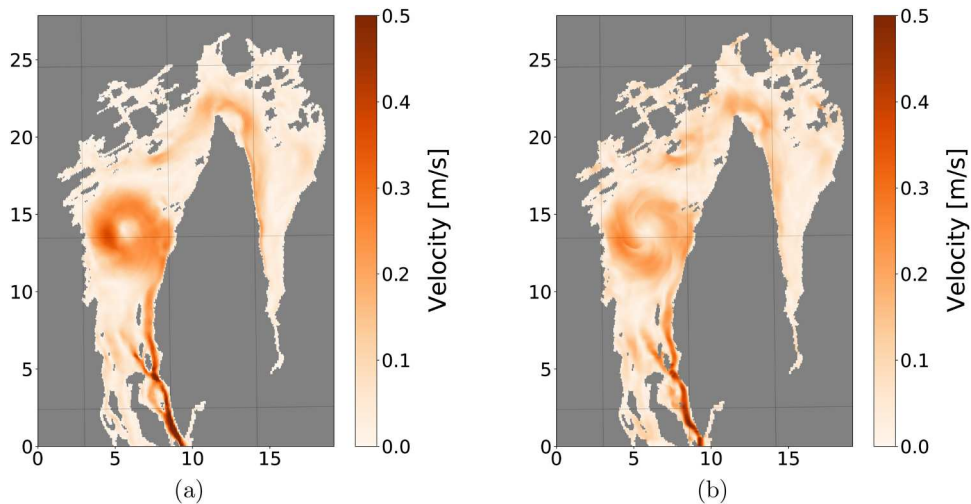


**Figure 4.** Absolute velocities of the currents in the barotropic model in the Oslofjord at the same point in time and with the same MLD criterion. The left panel shows the currents as initialised directly from FjordOs, whereas the right panel was initialised one hour earlier and simulated for one hour. (a) FjordOS and (b) Baroclinic model.

**Table 1.** Wall run times to simulate 1 h in the inner Oslofjord with different models.

	ROMS (2 nodes/4 CPUs/ 64 cores)		GPU Ocean (Single GPU)	
	Full 3D	Barotropic 2D	Barotropic 2D	Baroclinic 2D
Run time	923.1 s	53.1 s	2.65 s	0.083 s
Relative to GPU Ocean barotropic	349.0	20.1	1	0.031
Relative to GPU Ocean baroclinic	11,122.3	639.4	31.9	1

These simulations were run on two nodes with a total of 64 cores divided on four Intel Xeon Gold model 6130 (2.1 GHz) CPUs, connected with Intel OmniPath (100 Gbit/s).

Table 1 summarise the results, where we see that the ROMS models on 64 CPU cores with a total CPU time of more than 16 min for full 3D simulation, and just below 1 min for the barotropic 2D simulation. We note that overhead due to MPI communication in the ROMS model simulations is about 15 and 30 percent, respectively, of the total run time for the full 3D and barotropic 2D test cases. This is about 350 times longer for the full 3D ROMS simulation, and about 20 times longer for the barotropic 2D ROMS simulation than the GPU-accelerated barotropic model, which again requires about 32 times longer to run compared to the GPU-accelerated baroclinic model. For our two simplified models, the CFL restrictions depend on the phase speeds  $c_{\max} \approx \sqrt{gh_{\max}}$ , which for these cases have a ratio at about 32.6.

#### 4. Ensemble prediction for drift trajectories

We will now use the simplified models to make short-term ensemble predictions for drift trajectories in three different areas in Norway, see Figure A3(a) for details. These cases demonstrate how the barotropic and baroclinic processes contribute to a varying degree to the drift in different areas, and showcase how a standard barotropic shallow-water model, a reduced-gravity model, or a combination of both can serve as simplified models for drift predictions. In all three cases, we use simulation results from ROMS 3D models for initial and boundary conditions, and carry out sensitivity studies to identify how the different parameters in the models contribute to ensemble spread. We determine parameter ranges for the ensemble simulations by looking at the variances in the velocity field throughout each domain and the spread in selected drift trajectories with respect to the individual parameters. Moreover, we use OpenDrift (Dagestad et al. 2018) to produce reference trajectories using the uppermost layer from the ROMS

3D model simulations. Within OpenDrift, we simply use the OceanDrift model, and we generate references using three different leeway coefficients.

The operational ocean forecasts from MET Norway are made with the Norkyst-800 modelling system (Albretsen et al. 2011), which is based on the ROMS (Shchepetkin and McWilliams 2005) general circulation model. Herein, we use the NorFjords-160 and FjordOs model systems as our references, both of which are one-way nested into Norkyst-800. NorFjords-160 is a collection of 13 model domains that cover the entire Norwegian coastline with a grid resolution of 160 m each. FjordOs is an operational high-resolution ROMS-model for the Oslofjord as described in Røed et al. (2016) where the authors also highlight the benefits of high spatial resolution for complex topographies. It uses a curvilinear grid with horizontal resolution within the inner Oslofjord of 50 – 100 m. NorKyst-800 forecasts<sup>3</sup> and FjordOs hindcast<sup>4</sup> are available through MET Norway’s THREDDS Data Server, and NorFjords data is freely available upon request.

In the following, we initialise ensembles of simplified models using the same grid resolution as NorFjords-160 for North Cape and the Boknafjord, and project the FjordOs curvilinear gridded data onto a 50 m uniform grid for the Oslofjord. To illustrate that the ensembles are light-weight, all experiments are carried out on a single GPU and we use the available GPU memory as an upper constraint on the ensemble size. To further increase ensemble size or computational speed, spreading the ensemble across multiple GPUs using MPI is a viable option (Holm, Sætra, and Brodtkorb 2020).

$$\bar{h}u = \int_{-\zeta}^0 u - \tilde{u} dz \quad \text{and} \quad \bar{h}v = \int_{-\zeta}^0 v - \tilde{v} dz,$$

##### 4.1. North cape

The first example showcases the shallow-water model as described in Section 2.1. In the open waters of the Barents Sea, density anomalies are typically small and barotropic dynamics often dominate. Hence, we are unable to initialise reduced-gravity models based on our framework in this area, and therefore construct an ensemble of barotropic simplified models only. We focus on a chosen area just outside of North Cape. The reference initial conditions together with the initial placement of drifters can be seen in Figure A4(a).

##### 4.1.1. Barotropic parameter sensitivity study

We start by analysing the sensitivity of the model result with respect to perturbations of each parameter based

**Table 2.** Uncertain parameters and their perturbations as used in the barotropic sensitivity study and the trajectory forecasts outside of North Cape.

Sim	Parameter	Fixed value	Uncertainty spans			
			(Sensitivity study)		(Trajectory forecast)	
Barotropic	initial conditions	10:00	[00:00, 17:00]	18	[00:00, 17:00]	6
Barotropic	wind rotation	0°	[−45°, 45°]	19	[−10°, 10°]	5
Drift advection	windage, $\psi$	0.0	[0, 0.05]	11	$\mathcal{N}_+(0.03, 0.015)$	10

on our discussion in Section 2.4. To do so, we run a set of simulations with equidistant values for the individual uncertain parameters within their respective ranges, while keeping the other parameters fixed. Table 2 lists the uncertain parameters and their values. We then evaluate the sensitivity to the model results by looking at the variance in water velocity and the spread in the obtained drift trajectories after six hours. Note that we use no windage as a reference to more clearly investigate how the other uncertain parameters affect the ocean state directly.

Figure 5 shows the results of the barotropic sensitivity analysis. Note that there is an eddy centred approximately at (60, 40) in the figures. With time-shifted initial conditions in Figure 5(a), the spread in water velocity is especially strong around the eddy and at the upper boundary where tidal signals enter the domain. In contrast, Figure 5(b) shows that the wind response is too slow to generate significant spread in the ocean states. If we use windage with leeway coefficient  $\psi > 0$ , however, the different wind directions will give a larger spread in the trajectories through the direct wind drag on the drifters such that we still want to include a reasonable number of wind directions into a drift ensemble. This behaviour is illustrated by Figure 5(c), where we see the large effect of windage for a non-rotated wind field.

#### 4.1.2. Barotropic drift trajectory simulations

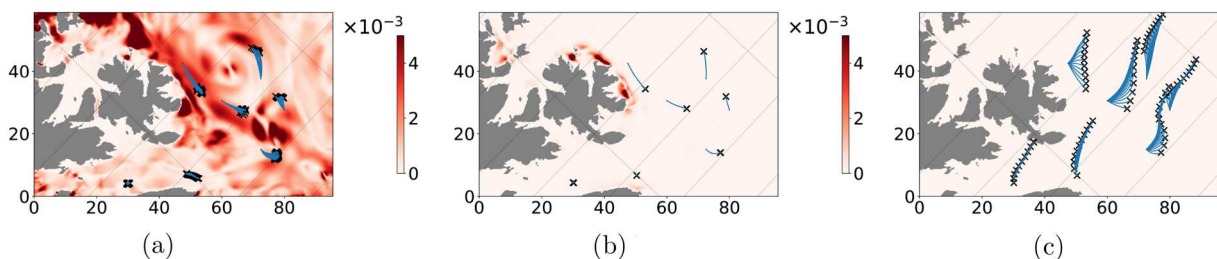
For the actual drifter experiment, we build an ensemble consisting of 30 barotropic models by mixing six different initial conditions and five wind rotations. Note that we have reduced the uncertainty in the wind direction here, compared to the values used in the sensitivity

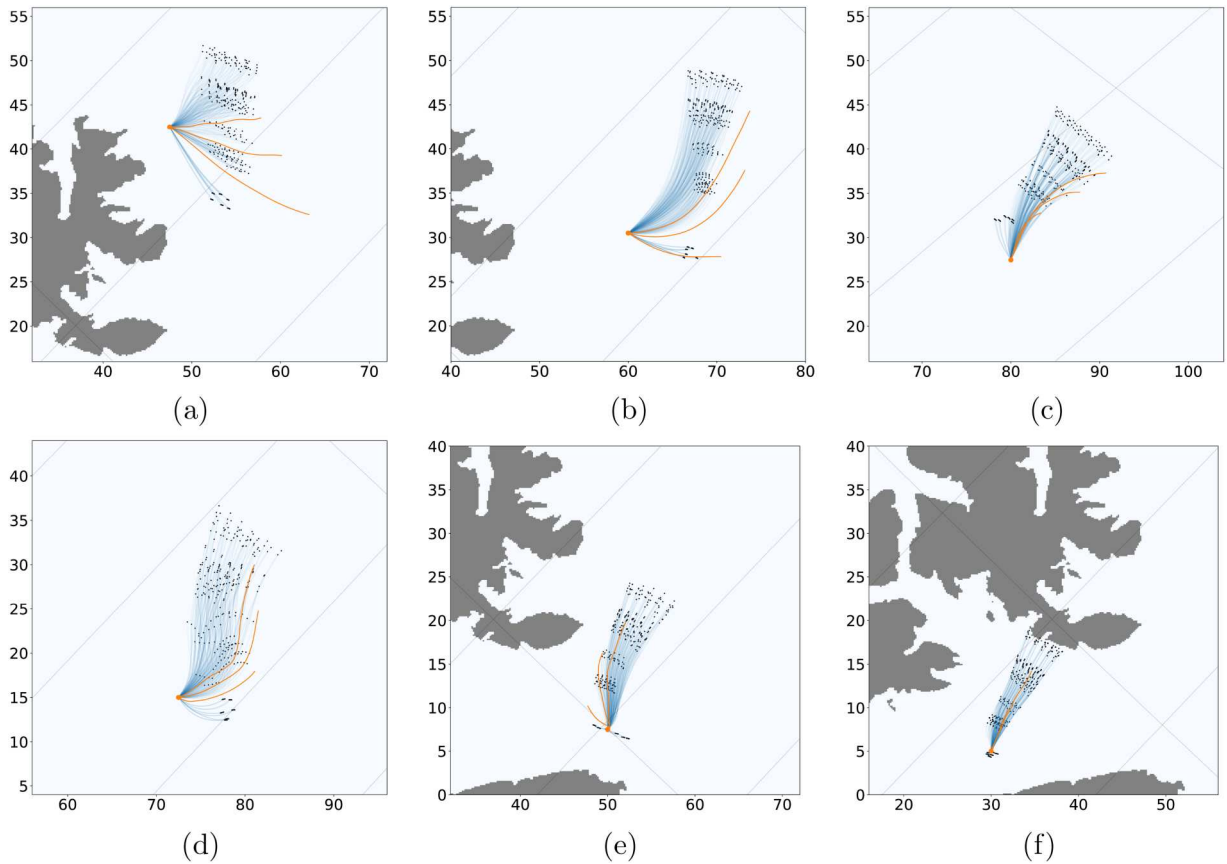
study. In addition, we add drifters with ten different leeway coefficients to each ensemble member, which are generated as positive realizations from a Gaussian distribution. Thus, we produce 300 drift trajectories in total.

Figure 6 shows the resulting drift trajectories. For drifter A and B, the ROMS reference lies outside the ensemble, while for all other starting positions they are covered by the ensemble spread and with the exception of drifter A, all paths in the ensemble follow similar shapes as the references. In general, the ROMS trajectories are longer than those from our ensemble, which is due to the surface currents being stronger than our depth averaged currents. It is clear that our barotropic model does not capture all dynamical features relevant for the drift. The currents in the ROMS 3D model are not entirely barotropic, as can be seen in Figure A4. In spite of these shortcomings, the barotropic ensemble modelling results are quite good. We recognise a clustering in the trajectories of drifter A, which is due to the leeway factors. This effect is less pronounced in the other cases, where the wind direction is not orthogonal to the current direction. Drifter F is mostly wind driven, since the currents at the entrance of the Porsangerfjord are weak, and we note that the ROMS reference lies in the middle of the ensemble.

#### 4.2. Inner Oslofjord

As we saw in Section 3, baroclinic dynamics dominates in the inner Oslofjord, with minimal contribution from the barotropic currents. As a consequence, we use an ensemble of reduced-gravity models only to predict drift trajectories in this area, and we start again by

**Figure 5.** Sensitivity to varying individual parameters in the barotropic model. The background fields in (a) and (b) show variance in water velocity, and all axes are in km. (a) Timeshifted initial conditions (b) Wind rotation and (c) Windage.



**Figure 6.** Barotropic drifter ensemble simulations for selected drifters. The orange trajectories are deterministically calculated using the the surface currents from NorFjords and OpenDrift with leeway factors 0%, 1.5% and 3%. All axes are in km. (a) Drifter A, (b) Drifter B, (c) Drifter C, (d) Drifter D, (e) Drifter E and (f) Drifter F.

investigating how much influence each uncertain parameter has on the resulting ocean states of the reduced-gravity model and the drift trajectories.

#### 4.2.1. Baroclinic parameter sensitivity study

Table 3 shows the parameters of the baroclinic model that we perturb. As discussed in Section 2.4, the initial MLD and the value of the reduced gravitational constant  $g'$  are coupled, but we evaluate the model's sensitivity to perturb  $g'$  alone while keeping the initial MLD fixed, and to perturb the MLD alone with  $g'$  fixed, since we do introduce errors in the signal phase speeds by

decoupling the modes. Moreover, we test the model sensitivity to the inter-layer friction, wind directions, and wind stress factors. Figure 7 shows the potential density of the upper 25 m along a south-north cut, along with five different isopycnals. The pycnocline is generally above 10 m depth.

Figure 8 show the result of the sensitivity analysis for the reduced-gravity model. The wind direction has limited influence on the circulation. The winds in this case are moderate, and the wind stress perturbation leads to a modest spread of the drifters in the wind direction. The perturbation of the interface friction causes the

**Table 3.** Uncertain parameters and their perturbations used in the baroclinic sensitivity study and trajectory forecast for the inner Oslofjord.

Sim	Parameter	Fixed value	Uncertainty spans			
			(Sensitivity study)	(Trajectory forecast)		
Baroclinic	wind rotation	0°	[−45°, 45°]	19	[−10°, 10°]	} 36
Baroclinic	wind stress factor, $\tau_0$	0.75	[0.1, 1.0]	10	$\mathcal{N}_+(0.35, 0.2)$	
Baroclinic	inter-layer friction, $\bar{\tau}$	0.003	[0, 0.005]	11	$\mathcal{N}_+(0.0025, 0.001)$	
Baroclinic	MDL criterion, $\rho$	1024.0	[1022.0, 1024.5]	6	$\mathcal{U}[1022.5, 1024.5]$	
Baroclinic	reduced gravity from MDL, $g'$	0.023	[0.020, 0.032]	6		
Baroclinic	reduced gravity set directly, $g'$	0.023	[0.01, 0.10]	10		
Drift advection	windage, $\psi$				$\mathcal{N}_+(0.03, 0.015)$	10

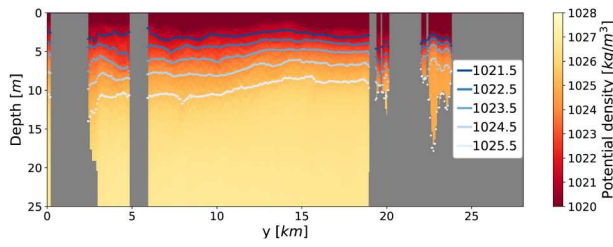


**Figure 7.** Isopycnals for a cross section along the  $y$ -axis through the strait of the ‘S5’-location in the Oslofjord (see Figure 2(a) for location).

largest variations in the ensemble. Perturbations of the MLD and the reduced gravity have limited influence on ensemble spread, with little difference between the coupled and decoupled treatment of the two parameters.

#### 4.2.2. Baroclinic drift trajectory simulations

From the baroclinic parameter sensitivity study, we infer reasonable parameter distributions for the construction of a baroclinic ensemble, as summarised in Table 3. We neglect the decoupled sampling of MLD and  $g'$ , since it results in little variability, and will only

use the coupled MLD and  $g'$ . For wind stress, inter-layer friction and MLD criterion, we now sample values from positive Gaussian and uniform distributions, in contrast to the parameter study where we fixed equidistant values within selected ranges. For the wind rotation, however, we still use fixed equidistant values, due to technical constraints in how the wind forcing is implemented in the GPU framework. We take advantage of the fact that the reduced-gravity models runs significantly faster than the barotropic models, and use a relatively large ensemble. In total, we consider 270 baroclinic simulations and ten leeway factors per instance.

In Figure 9, we show the ensemble trajectory predictions for each drifter. For drifter A, all three reference trajectories from ROMS strand eventually, together with a big share of the ensemble members. For drifters B, C and F, the ensemble spread is dominated by the spread in the wind direction, but lies around the reference trajectories. The drifter D trajectories bifurcates, and interestingly this is evident in both the ensemble and the ROMS reference simulations. For drifter E, the reference simulations fall outside of the ensemble, which is due to unresolved near-surface vertical velocity shear in the reduced-gravity model ensemble.

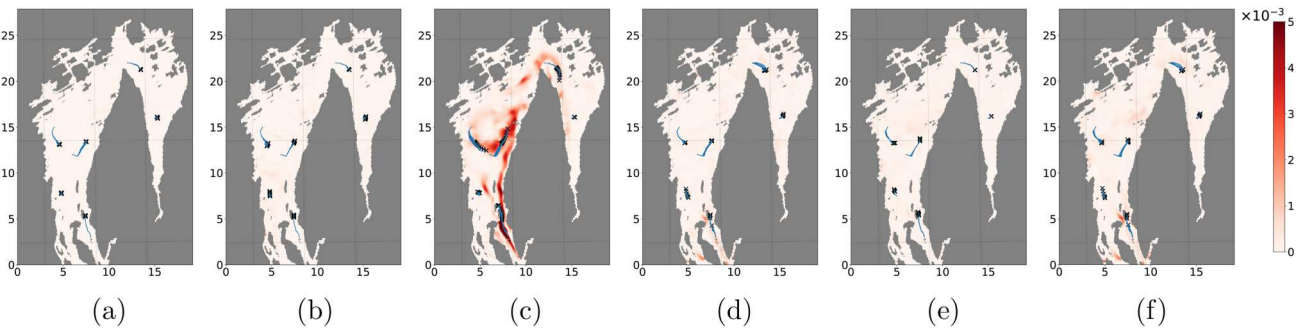


**Figure 8.** Sensitivity to varying individual parameters in the reduced-gravity model. The background fields show variance in water velocity, with axes in km. (a) Wind rotation, (b) Wind stress, (c) Friction, (d) MLD and  $g'$ , (e)  $g'$  and (f) MLD.

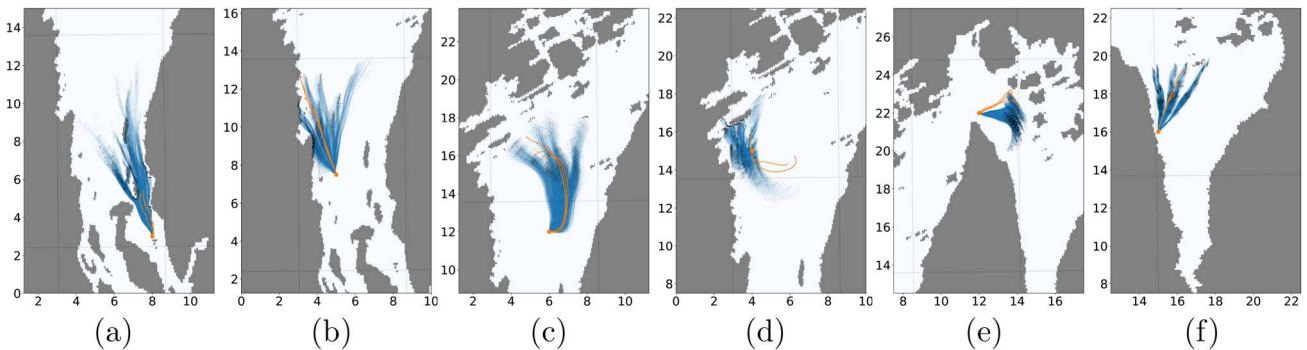


**Figure 9.** Baroclinic drifter ensemble simulation zoomed in on each individual drifter. Orange trajectories come from OpenDrift using FjordOs surface currents and leeway factors 0%, 1.5% and 3%. The axes are in km. (a) Drifter A, (b) Drifter B, (c) Drifter C, (d) Drifter D, (e) Drifter E and (f) Drifter F.

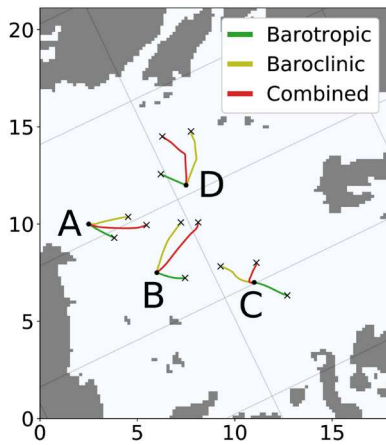


**Figure 10.** Deterministic drift trajectories calculated with different simplified models and leeway coefficient  $\psi = 0$ . Axes are in km.

**Table 4.** Uncertain parameters and their perturbations used in the combined sensitivity study and trajectory forecast in the Boknafjord.

Sim	Parameter	Uncertainty sampling	
Barotropic	wind rotation	$[-10^\circ, 10^\circ]$	5
Barotropic	initial condition	[05:00, 17:00]	3
Baroclinic	wind rotation	$[-10^\circ, 10^\circ]$	5
Baroclinic	wind stress factor, $\tau_0$	$\mathcal{N}_+(0.35, 0.25)$	} 36
Baroclinic	inter-layer friction, $\bar{\tau}$	$\mathcal{N}_+(0.0025, 0.001)$	
Baroclinic	MDL criterion, $\rho$	$\mathcal{U}[1022.75, 1023.5]$	
Drift advection	windage, $\psi$	$\mathcal{N}_+(0.03, 0.015)$	10

### 4.3. Boknafjord

The third example is from the Boknafjord just north of Stavanger. Here we find that both barotropic and baroclinic currents play a significant role for the drift, and the drift predictions are based on adding currents from the barotropic and baroclinic models.

This is shown by Figure 10, where we have plotted deterministic trajectories using the barotropic, the baroclinic, and the combined model for four drifters. In particular, drifter D has a  $180^\circ$  difference between the trajectories from the two individual models, and for drifters B and D, this difference is on  $90^\circ$ . This underlines that neglecting either of the signals results in a loss of information. By using the combined current from both simplified models, we get deterministic trajectories that lie in between the individual models.

#### 4.3.1. Parameter sensitivity study

Similarly to the two former cases, we carry out a parameter sensitivity study. Table 4 lists the relevant parameters, where the most important differences from the previous cases are the sensitivities related to the initial MLD. The pycnocline in the Boknafjord is well defined, but the stratification is weaker than in the

Oslofjord. Hence, small changes in the MLD density criterion significantly change the resulting depth of the mixed layer. The span of the densities for the MLD is therefore here adapted to a smaller interval. Furthermore, a shallow MLD responds more strongly to variations in the wind, which means that the effects of the MLD perturbations on the drift are not expected to be symmetrically distributed around the MLD average. The MLD is in general more shallow in the south-western part of the domain (left side of the plots) and deeper in the north (top right in the plots).

#### 4.3.2. Combined drift trajectory simulations

We use ensembles of 15 barotropic and 180 baroclinic members, respectively. In addition, we sample ten leeway coefficients per member, which results in 27,000 combined trajectories in total for each of the four drifters. Figure 11 shows the resulting forecasted trajectories, where the top row shows all individual trajectories and the bottom row shows the probability distribution through estimated kernel densities for the drifters' final positions after six hours. It should be noted that the wind direction without rotation is roughly parallel to the  $y$ -axis. Since the currents of the barotropic and baroclinic model in general are not aligned, we get a noticeable increase in the trajectory spread. Furthermore, we see that for drifters B and C in particular, the reference trajectories based on the ROMS model and OpenDrift go in the direction of the deterministic combined trajectories from Figure 10. By looking at the ensemble trajectories, we see that the characteristics of the reference trajectories are represented in the ensembles. For all drifters except for drifter C, the reference trajectories are within the 90% confidence area of the ensemble distribution, illustrating the potential of the combination of our approach.

## 5. Discussion

The starting point of this paper was a GPU-accelerated framework for running ensembles of barotropic simplified ocean models intended for short-term drift trajectory predictions in real-world domains based on the shallow-water equations. In this paper, we have presented how the framework can be expanded to also run ensembles of baroclinic reduced-gravity models by reusing the underlying computational code. Furthermore, since the phase speeds of reduced-gravity models are much smaller than their barotropic counterparts, we can increase the temporal step sizes of the models significantly which give increased computational performance. We have also proposed to

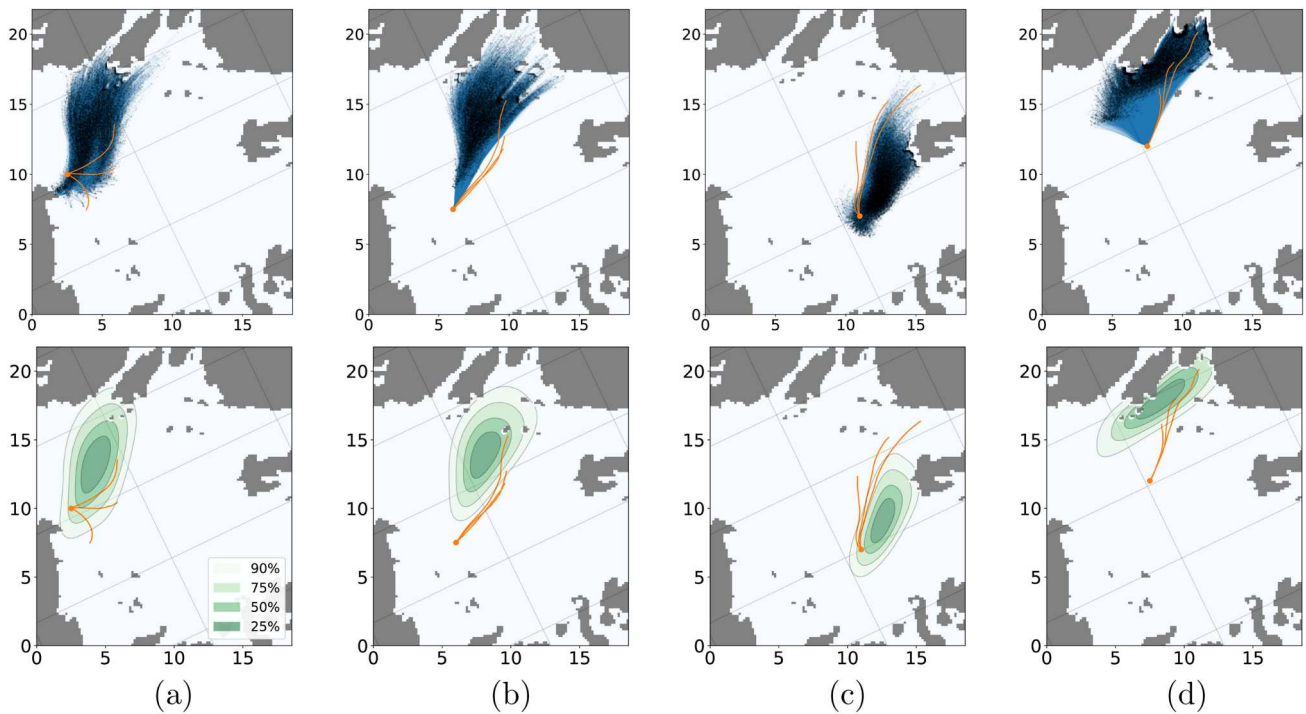


**Figure 11.** Ensemble drift forecast made from the combined simplified model in the Boknafjord. The trajectories are shown at the top, and the probability distribution after six hours at the bottom. Orange trajectories are computed by OpenDrift using NorFjords surface currents and leeway factors 0%, 1.5% and 3%. The axes are in km. (a) Drifter A, (b) Drifter B, (c) Drifter C and (d) Drifter D.

simulate drift trajectories using a combination of the barotropic and reduced-gravity models, and shown how we can form large drift trajectory ensembles by combining the simulated currents from any pair of models from an ensemble of barotropic models and an ensemble of reduced-gravity models. To demonstrate the use of both barotropic and baroclinic simplified models, we presented drift trajectory simulations for three different areas along the Norwegian coast. The examples show barotropic-dominated currents (North Cape), currents dominated by baroclinic dynamics (Oslofjord), and contributions from both (Boknafjord). We also discussed the sensitivity to uncertain parameters for all cases and presented several ensemble simulations for a range of numerical drifters with different initial positions. Our results show that the ensemble spread generated by the simplified models most often cover the deterministic trajectories we used as reference solutions, which are computed from the surface currents from a 3D general circulation model.

In a real-world setting, the underlying assumptions on which the simplified models are based are certainly not always fulfilled. The self-imposed constraint of reusing very efficient existing numerical solvers forces us to make compromises with regard to model complexity and accuracy. There are issues with defining the MLD, especially in cases without a well-defined pycnocline,

and in shallow waters where the assumption of a deep lower layer is clearly invalid, we cannot expect the reduced-gravity model to perform well. We want to reiterate, however, that our primary aim is not to replace full 3D circulation models and provide accurate descriptions of the state of the ocean. Our goal is rather to use the simplified models to provide additional tools for decision support when short term forecasts of surface drift are needed. Our main region of interest is the Norwegian coastal zone, which is complex both in terms of topography and freshwater forcings. In most cases of practical interest, incidents happen close to land where the main source of error in our conventional ocean forecasting system is lack of spatial resolution. With the numerical tools presented here, it is straightforward to spawn large ensembles of simplified models with very high resolution, combining robust physics for the barotropic dynamics with a more rudimentary description of the MLD dynamics, but which at least provide the opportunity to estimate the lowest order baroclinic mode.

For drift trajectory modelling, the input data from ocean models contributes significantly to the total uncertainty, and it is our hope that the simplified models we present here can be integrated as additional tools in the operational production chain. It remains, of course, to study carefully how these tools perform under a variety of environmental conditions so that

their use is limited to cases where they add value. This also includes a more sophisticated and robust analysis of the uncertainty ranges for creating realistic ensemble spread. In this study, we have used very simple models for the complex coastal ocean dynamics that are better captured by fully 3D circulation models. As mentioned in the introduction, our simplified models need only be reasonably accurate on the short timescales relevant to decision support and in situations that are suitable for rapid update cycling, but more research is needed on better initialisation procedures and improved model physics, ideally using coupled modes if efficient implementations can be made on heterogeneous computing platforms. Finally, we would like to stress that large ensembles of these low-dimensional simplified models are particularly well suited for fully nonlinear data assimilation methods (Van Leeuwen 2009; Holm, Sætra, and Brodtkorb 2020), which is relevant for accurate short term drift forecasting in situations where the position of the object is known from, e.g. GPS-trackers.

## Notes

1. The simulation framework has mainly been developed using ocean forecasts from the NorKyst-800 model (Albretsen et al. 2011) that is operationally run by the Norwegian Meteorological Institute. Other forecast models have been tested as well, and in this study in particular, we use data from NorFjords-160 and FjordOs (Røed et al. 2016), the latter focuses on the Oslofjord.
2. This can be done in multiple ways. We have used the EOS80 module in the Python package `seawater` (Fernandes 2015), which implements Fofonoff and Millard (1983) for the purpose.
3. <https://thredds.met.no/thredds/fou-hi/norkyst800v2.html>.
4. Catalog can be found at [https://thredds.met.no/thredds/catalog/fjordos/fjordos\\_2\\_hindcast/v6/exp1/catalog.html](https://thredds.met.no/thredds/catalog/fjordos/fjordos_2_hindcast/v6/exp1/catalog.html).

## Disclosure statement

No potential conflict of interest was reported by the author(s).

## Funding

This work is supported by the Research Council of Norway [Norges Forskningsråd] [grant number 310515] (Havvarsel).

## Code availability

The source code used to produce the results presented in this paper is available under a GNU free and open source license in order to enhance scientific exchange. The numerical results can be reproduced using Jupyter notebooks at <https://doi.org/10.5281/zenodo.11504834>.

The simplified models and GPU-accelerated framework GPU Ocean can be found on <https://github.com/gpuocean/gpuocean>, and the results are made using the version 1.2.0 at <https://doi.org/10.5281/zenodo.11502401>.

## Notes on contributors

*Florian Beiser* is a PhD student within the Applied Computational Sciences research group at SINTEF Digital, where his research focusses on drift trajectory forecasting with simplified ocean models and data assimilation.

*Håvard Heitlo Holm* is a research scientist within the Applied Computational Sciences research group at SINTEF Digital. His research focuses on developing GPU-accelerated simplified ocean models for forecasting real-world drift trajectories with associated uncertainty quantification. This also includes to make use of available observations through ensemble-based data assimilation methods.


*Martin Lilleeng Sætra* is a research scientist with the Norwegian Meteorological Institute. Martin does research in accelerated scientific computing, numerical simulation, and scientific visualization. His recent projects involve drift trajectory forecasts based on GPU-accelerated simplified ocean models, ensemble prediction systems, and data assimilation methods. He also holds an adjunct position at the Department of Computer Science, Oslo Metropolitan University.

*Nils Melsom Kristensen*, responsible for operational storm surge modelling at MET Norway, and has extensive knowledge and experience in high resolution coastal ocean modelling.

*Kai Håkon Christensen* works as a senior scientist at the Norwegian Meteorological Institute, and his main research topics are air-sea interaction processes, high resolution numerical circulation modeling, and ocean data assimilation. He also holds an adjunct position at the Dept. of Geosciences, Univ. Oslo.

## ORCID

*Florian Beiser*  <http://orcid.org/0000-0001-5579-749X>

*Håvard Heitlo Holm*  <http://orcid.org/0000-0002-2328-9447>

*Martin Lilleeng Sætra*  <http://orcid.org/0000-0002-9932-7200>

*Nils Melsom Kristensen*  <http://orcid.org/0000-0002-2494-6509>

*Kai Håkon Christensen*  <http://orcid.org/0000-0002-5775-794X>

## References

- Albretsen J, Sperrevik A, Staalstrøm A, Sandvik A, Vikebø F, Asplin L. 2011. NorKyst-800 report no. 1 user manual and technical descriptions. *Fisken Og Havet*. 2:1–48.
- Arango H, Reid R. 1991. A generalized reduced-gravity ocean model. *Atmosphere-Ocean*. 29(2):256–287. doi: [10.1080/07055900.1991.9649405](https://doi.org/10.1080/07055900.1991.9649405)



- Beiser F, Holm H, Eidsvik J. 2023. Comparison of ensemble-based data assimilation methods for sparse oceanographic data. *Q J R Meteorol Soc.* 150:1068–1095. doi: [10.1002/qj.v150.759](https://doi.org/10.1002/qj.v150.759)
- Bleck R. 2002. An oceanic general circulation model framed in hybrid isopycnic-Cartesian coordinates. *Ocean Modell.* 4(1):55–88. doi: [10.1016/S1463-5003\(01\)00012-9](https://doi.org/10.1016/S1463-5003(01)00012-9)
- Brainerd K, Gregg M. 1995. Surface mixed and mixing layer depths. *Deep Sea Res Part I: Oceanographic Research Papers.* 42(9):1521–1543. doi: [10.1016/0967-0637\(95\)00068-H](https://doi.org/10.1016/0967-0637(95)00068-H)
- Brodtkorb A, Holm H. 2021. Coastal ocean forecasting on the GPU using a two-dimensional finite-volume scheme. *Tellus, Ser A: Dynamic Meteorology and Oceanography.* 73(1):1–22. doi: [10.1080/16000870.2021.1876341](https://doi.org/10.1080/16000870.2021.1876341)
- Brodtkorb A, Holm H, Sætra M, Beiser F. 2024. *GPU Ocean, version v1.2.0*. Zenodo. doi: [10.5281/zenodo.11502401](https://doi.org/10.5281/zenodo.11502401)
- Brodtkorb A, Sætra M, Altinakar M. 2012. Efficient shallow water simulations on GPUs: implementation, visualization, verification, and validation. *Comput Fluids.* 55:1–12. doi: [10.1016/j.compfluid.2011.10.012](https://doi.org/10.1016/j.compfluid.2011.10.012)
- Castro-Díaz M, Fernández-Nieto E, González-Vida J, Parés-Madroñal C. 2011. Numerical treatment of the loss of hyperbolicity of the two-layer shallow-water system. *J Sci Comput.* 48(1):16–40. doi: [10.1007/s10915-010-9427-5](https://doi.org/10.1007/s10915-010-9427-5)
- Chassignet E, Smith L, Halliwell G, Bleck R. 2003. North Atlantic simulations with the hybrid coordinate ocean model (HYCOM): impact of the vertical coordinate choice, reference pressure, and thermobaricity. *J Phys Oceanogr.* 33(12):2504–2526. doi: [10.1175/1520-0485\(2003\)033<2504:NASWTH>2.0.CO;2](https://doi.org/10.1175/1520-0485(2003)033<2504:NASWTH>2.0.CO;2)
- Chertock A, Dudzinski M, Kurganov A, Lukáčová-Medvid'ová M. 2018. Well-balanced schemes for the shallow water equations with Coriolis forces. *Numerische Mathematik.* 138(4):939–973. doi: [10.1007/s00211-017-0928-0](https://doi.org/10.1007/s00211-017-0928-0)
- Christensen K, Breivik O, Dagestad K, Röhrs J, Ward B. 2018. Short-term predictions of oceanic drift. *Oceanography.* 31(3):59–67. doi: [10.5670/oceanog.2018.310](https://doi.org/10.5670/oceanog.2018.310)
- Dagestad K-F, Röhrs J, Breivik Ø, Ådlandsvik B. 2018. OpenDrift v1.0: a generic framework for trajectory modeling. *Geosci Model Dev.* 11(4):1405–1420. doi: [10.5194/gmd-11-1405-2018](https://doi.org/10.5194/gmd-11-1405-2018)
- Davies H. 1976. A lateral boundary formulation for multi-level prediction models. *Q J R Meteorol Soc.* 102(432):405–418.
- de Boyer Montégut C, Madec G, Fischer A, Lazar A, Iudicone D. 2004. Mixed layer depth over the global ocean: an examination of profile data and a profile-based climatology. *J Geophys Res: Oceans.* 109(C12):C12003–1–C12003–20.
- de la Asunción M, Castro M, Mantas J, Ortega S. 2016. Numerical simulation of tsunamis generated by landslides on multiple GPUs. *Adv Eng Softw.* 99:59–72. doi: [10.1016/j.advengsoft.2016.05.005](https://doi.org/10.1016/j.advengsoft.2016.05.005)
- de la Asunción M, Mantas J, Castro M. 2011. Simulation of one-layer shallow water systems on multicore and CUDA architectures. *J Supercomput.* 58(2):206–214. doi: [10.1007/s11227-010-0406-2](https://doi.org/10.1007/s11227-010-0406-2)
- Dellar P, Salmon R. 2005. Shallow water equations with a complete coriolis force and topography. *Phys Fluids.* 17(10):106601. doi: [10.1063/1.2116747](https://doi.org/10.1063/1.2116747)
- Dong T, Dobrev V, Kolev T, Rieben R, Tomov S, Dongarra J. 2014. A step towards energy efficient computing: Redesigning a hydrodynamic application on CPU-GPU. In: 2014 IEEE 28th International Parallel and Distributed Processing Symposium. Phoenix: IEEE; p. 972–981.
- Dyakonova T, Khoperskov A. 2018. Bottom friction models for shallow water equations: manning's roughness coefficient and small-scale bottom heterogeneity. *J Phys: Conf Ser.* 973(1):012032.
- Fernandes. 2015. python-seawater v3.3.2.
- Fofonoff P, Millard R. 1983. Algorithms for computation of fundamental properties of seawater. UNESCO technical papers in marine science, 44.
- Gent P, Cane M. 1989. A reduced gravity, primitive equation model of the upper equatorial ocean. *J Comput Phys.* 81(2):444–480. doi: [10.1016/0021-9991\(89\)90216-7](https://doi.org/10.1016/0021-9991(89)90216-7)
- Giunta V, Ward B. 2022. Ocean mixed layer depth from dissipation. *Journal of Geophysical Research: Oceans.* 127(4):e2021JC017904– doi: [10.1029/2021JC017904](https://doi.org/10.1029/2021JC017904)
- Gottlieb S, Shu C-W. 1998. Total variation diminishing Runge-Kutta schemes. *Math Comput.* 67(221):73–85. doi: [10.1090/mcom/1998-67-221](https://doi.org/10.1090/mcom/1998-67-221)
- Hjelmervik K, Kristensen N. 2019. The Oslo fjord ocean model: communication and applications. In: OCEANS 2019-Marseille. Marseille: IEEE; p. 1–5.
- Holm H, Brodtkorb A, Broström G, Christensen K, Sætra M. 2020. Evaluation of selected finite-difference and finite-volume approaches to rotational shallow-water flow. *Commun Comput Phys.* 27(4):1234–1274. doi: [10.4208/cicp.OA-2019-0033](https://doi.org/10.4208/cicp.OA-2019-0033)
- Holm H, Sætra M, Brodtkorb A. 2020. Data assimilation for ocean drift trajectories using massive ensembles and GPUs. In: Klöfkor R, Keilegavlen E, Radu F, and Fuhrmann J, editors. Finite volumes for complex applications IX – methods, theoretical aspects, examples. Cham: Springer International Publishing; p. 715–723.
- Holm H, Sætra M, van Leeuwen P. 2020. Massively parallel implicit equal-weights particle filter for ocean drift trajectory forecasting. *J Comput Phys: X.* 6(0314):100053.
- Huang S, Xiao S, Feng W-C. 2009. On the energy efficiency of graphics processing units for scientific computing. In: 2009 IEEE International Symposium on Parallel & Distributed Processing. Chengdu: IEEE; p. 1–8.
- Kim C-H, Yoon J-H. 1996. Modeling of the wind-driven circulation in the Japan sea using a reduced gravity model. *J Oceanogr.* 52:359–373. doi: [10.1007/BF02235930](https://doi.org/10.1007/BF02235930)
- Kristensen N, Røed L, Sætra Ø. 2022. A forecasting and warning system of storm surge events along the Norwegian coast. *Environmental Fluid Mech.* 23:307–329. doi: [10.1007/s10652-022-09871-4](https://doi.org/10.1007/s10652-022-09871-4)
- Kudryavtsev V, Monzikova A, Combet C, Chapron B, Reul N. 2019. A simplified model for the baroclinic and barotropic ocean response to moving tropical cyclones: 2. Model and simulations. *J Geophys Res: Oceans.* 124(5):3462–3485. doi: [10.1029/2018JC014747](https://doi.org/10.1029/2018JC014747)
- Large W, Pond S. 1981. Open ocean momentum flux measurements in moderate to strong winds. *J Phys Oceanogr.* 11:324–336. doi: [10.1175/1520-0485\(1981\)011<0324:OOMFMI>2.0.CO;2](https://doi.org/10.1175/1520-0485(1981)011<0324:OOMFMI>2.0.CO;2)

- Madec G and the NEMO team. 2008. NEMO Ocean Engine. Note du Pôle de modélisation, Institut Pierre-Simon Laplace (IPSL), France, No 27, ISSN No. 1288–1619.
- NVIDIA. 2023. NVIDIA CUDA C++ programming guide version 12.2.
- Peña-Molino B, Rintoul S, Mazloff M. 2014. Barotropic and baroclinic contributions to along-stream and across-stream transport in the antarctic circumpolar current. *Journal of Geophysical Research: Oceans*. 119(11):8011–8028. doi: [10.1002/2014JC010020](https://doi.org/10.1002/2014JC010020)
- Røed L. 2012. Documentation of simple ocean models for use in ensemble predictions. Part I: theory. Technical Report, Norwegian Meteorological Institute.
- Røed L. 2019. Atmospheres and oceans on computers. Cham: Springer International Publishing.
- Røed L, Kristensen N, Hjelmervik K, Staalstrøm A. 2016. A high-resolution, curvilinear ROMS model for the Oslofjord. FjordOs Technical report no. 2. Technical report, MET Norway.
- Röhrs J, Christensen K. 2015. Drift in the uppermost part of the ocean. *Geophys Res Lett*. 42(23):349–356.
- Röhrs J, Sutherland G, Jeans G, Bedington M, Sperrevik A, Dagestad K-F, Gusdal Y, Mauritzen C, Dale A, LaCasce J. 2023. Surface currents in operational oceanography: key applications, mechanisms, and methods. *J Oper Oceanogr*. 16(1):60–88.
- Samelson R, Chelton D, Schlax M. 2019. The ocean mesoscale regime of the reduced-gravity quasigeostrophic model. *J Phys Oceanogr*. 49(10):2469–2498. doi: [10.1175/JPO-D-18-0260.1](https://doi.org/10.1175/JPO-D-18-0260.1)
- Sanders J, Kandrot E. 2010. CUDA by example: an introduction to general-purpose GPU programming. Boston: Addison-Wesley Professional.
- Shchepetkin A, McWilliams J. 2005. The regional oceanic modeling system (ROMS): a split-explicit, free-surface, topography-following-coordinate oceanic model. *Ocean Modell*. 9(4):347–404. doi: [10.1016/j.ocemod.2004.08.002](https://doi.org/10.1016/j.ocemod.2004.08.002)
- Staalstrøm A, Aas E, Liljebladh B. 2012. Propagation and dissipation of internal tides in the Oslofjord. *Ocean Sci*. 8(4):525–543. doi: [10.5194/os-8-525-2012](https://doi.org/10.5194/os-8-525-2012)
- Støylen E, Fer I. 2014. Tidally induced internal motion in an Arctic fjord. *Nonlinear Process Geophys*. 21(1):87–100. doi: [10.5194/npg-21-87-2014](https://doi.org/10.5194/npg-21-87-2014)
- Sutherland G, Soontiens N, Davidson F, Smith G, Bernier N, Blanken H, Schillinger D, Marcotte G, Röhrs J, Dagestad K-F, et al. 2020. Evaluating the leeway coefficient of ocean drifters using operational marine environmental prediction systems. *J Atmospheric Oceanic Technol*. 37(11):1943–1954. doi: [10.1175/JTECH-D-20-0013.1](https://doi.org/10.1175/JTECH-D-20-0013.1)
- Van Leeuwen P. 2009. Particle filtering in geophysical systems. *Monthly Weather Rev*. 137(12):4089–4114. doi: [10.1175/2009MWR2835.1](https://doi.org/10.1175/2009MWR2835.1)
- van Sebille E, Aliani S, Law K, Maximenko N, Alsina J, Bagaev A, Bergmann M, Chapron B, Chubarenko I, Cózar A, et al. 2020. The physical oceanography of the transport of floating marine debris. *Environ Res Lett*. 15(2):023003. doi: [10.1088/1748-9326/ab6d7d](https://doi.org/10.1088/1748-9326/ab6d7d)
- Wang J, Ikeda M, Saucier F. 2003. A theoretical, two-layer, reduced-gravity model for descending dense water flow on continental shelves/slopes. *J Geophys Res: Oceans*. 108(C5):30-1–30-18.

## Appendices

### Appendix 1. Derivation of reduced-gravity model

Starting from the two-layer shallow-water equations, here shown with the momentum in  $x$ -direction only for simplicity,

$$\begin{aligned} & \begin{bmatrix} h_1 \\ h_1 u_1 \\ h_2 \\ h_2 u_2 \end{bmatrix}_t + \begin{bmatrix} h_1 u_1 \\ h_1 u_1^2 + \frac{1}{2} g h_1^2 \\ h_2 u_2 \\ h_2 u_2^2 + \frac{1}{2} g h_2^2 \end{bmatrix}_x = \begin{bmatrix} 0 \\ f h_1 v_1 \\ 0 \\ -f h_2 v_2 \end{bmatrix} + \begin{bmatrix} 0 \\ -g h_1 (h_2)_x \\ 0 \\ -g \delta h_2 (h_1)_x \end{bmatrix} \\ & + \begin{bmatrix} 0 \\ g h_1 H_x \\ 0 \\ g h_2 H_x \end{bmatrix} + \begin{bmatrix} 0 \\ \tau_u - r(u_1 - u_2)|u_1 - u_2| \\ 0 \\ r_1(u_1 - u_2)|u_1 - u_2| - r_2 u_2 |u_2| \end{bmatrix}. \end{aligned} \quad (A1)$$

The variables are sketched in Figure A1. Subscripts 1 and 2 denote upper and lower layers, respectively, and total equilibrium depth is  $H = H_1 + H_2$ . Let  $\eta$  and  $\zeta$  denote deviations

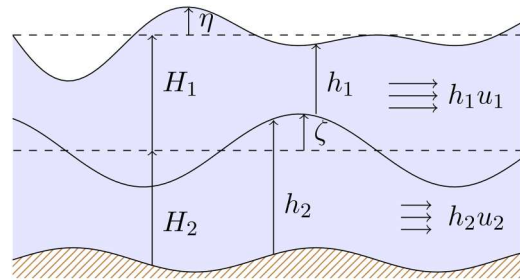


**Figure A1.** Two-level shallow-water model with variables and reference levels.

from equilibrium levels at the surface and layer interface, respectively, so that  $h_1 = H_1 + \eta - \zeta$  and  $h_2 = H_2 + \zeta$ . Furthermore,  $\tau_u$  is wind forcing, and  $r_1$  and  $r_2$  are the friction coefficients accounting for the shear stress between the layers and the bed friction, respectively. Finally,  $\delta = \rho_1/\rho_2 < 1$ , where  $\rho$  is water density.

To derive the baroclinic reduced-gravity model we first isolate the baroclinic response by enforcing  $\eta \equiv 0$ , which requires

$$h_1 u_1 = -h_2 u_2. \quad (A2)$$

Consequently, the mass conservation in both layers reduces to the same equation

$$(-\zeta)_t + (h_1 u_1)_x = 0. \quad (A3)$$

The resulting system of equations could also be a valid modeling approach, but would require very different numerical methods compared to those used herein.

Next, we assume that the lower layer is much deeper than the upper layer,  $h_1 \ll h_2$ . Using (A2) once again, this means that  $|u_2| \ll |u_1|$ , and we can think of the lower layer as almost stationary. With  $u_2, v_2 = 0$ , the momentum equation in the

lower layer in (A1) reduces to

$$\left(\frac{1}{2}gh_2^2\right)_x = -\delta gh_2(h_1)_x + gh_2H_x. \quad (\text{A4})$$

Using chain rule, this can be also written as

$$(h_2)_x \approx -\delta(h_1)_x + H_x. \quad (\text{A5})$$

By looking at only the gravitational terms in the momentum equation for the upper layer, while putting all other terms into  $F$  and plugging (A5) in, we get that

$$\begin{aligned} \left(\frac{1}{2}gh_1^2\right)_x &= -gh_1(h_2)_x + gh_1H_x + F, \\ gh_1(h_1)_x &= \delta gh_1(h_1)_x - gh_1H_x + gh_1H_x + F, \\ (1 - \delta)gh_1(h_1)_x &= F, \\ (1 - \delta)\left(\frac{1}{2}gh_1^2\right)_x &= F, \end{aligned} \quad (\text{A6})$$

where the forcing term from the bathymetry got cancelled out.

Finally, let  $g' = (1 - \delta)g = \frac{\rho_2 - \rho_1}{\rho_2}g$ . Note that we then can discard the momentum equation for the lower level in (A1), which leaves us with

$$\begin{aligned} \left[ \begin{array}{c} -\zeta \\ h_1 u_1 \end{array} \right]_t + \left[ \begin{array}{c} h_1 u_1 \\ h_1 u_1^2 + \frac{1}{2}g'h_1^2 \end{array} \right]_x \\ = \left[ \begin{array}{c} 0 \\ fh_1 v_1 \end{array} \right] + \left[ \begin{array}{c} 0 \\ \tau_u - r_1 u_1 |u_1| \end{array} \right]. \end{aligned} \quad (\text{A7})$$

By changing the orientation of  $\zeta$ , replacing all subscripts  $\cdot_1$  with bars  $\bar{\cdot}$ , and including the momentum in  $y$ -direction, this corresponds to the baroclinic reduced-gravity model in (4).

An alternative derivation can be found in Røed (2012, Sec. 2.7). There, it is also suggested to use a reduced gravity that

varies in space and time. The proposed reduced gravity would then take values in the interval  $[\frac{g'}{2}, g']$ . Seeing the low sensitivity with respect to an even larger uncertainty interval in Section 4, we neglect this suggestion in favour for re-using the code infrastructure of the barotropic model.

## Appendix 2. Internal Kelvin waves

Kelvin waves are coastally trapped through the Coriolis force and limited in spatial extent to within a Rossby radius of deformation from the coastline. In the northern hemisphere, Kelvin waves propagate with the coast to the right. For our applications with reduced-gravity models, it is the internal Kelvin wave and internal Rossby radius that are relevant. A practical example of such internal motion is studied for example in Støylen and Fer (2014). The internal Rossby radius is calculated from the reduced-gravity phase speed,  $c = \sqrt{g'H}$ , with a corresponding Rossby radius of  $R = c/f$ . We consider an idealised set-up to verify the simulation results by choosing a similar case to that presented in Holm, Brodtkorb et al. (2020).

We use a rectangular domain with size  $80 \text{ km} \times 120 \text{ km}$  with wall boundary conditions at the north and south boundaries, and a periodic boundary in east and west. The initial state is constructed as

$$\begin{aligned} \zeta(x, y, 0) &= \zeta_0 \exp\left(\frac{-\sqrt{(y-y_0)^2}}{R}\right) F(x), \\ hu(x, y, 0) &= c \cdot \text{sign}(y - y_0) \zeta(x, y, 0), \quad hv(x, y, 0) = 0, \end{aligned} \quad (\text{A8})$$

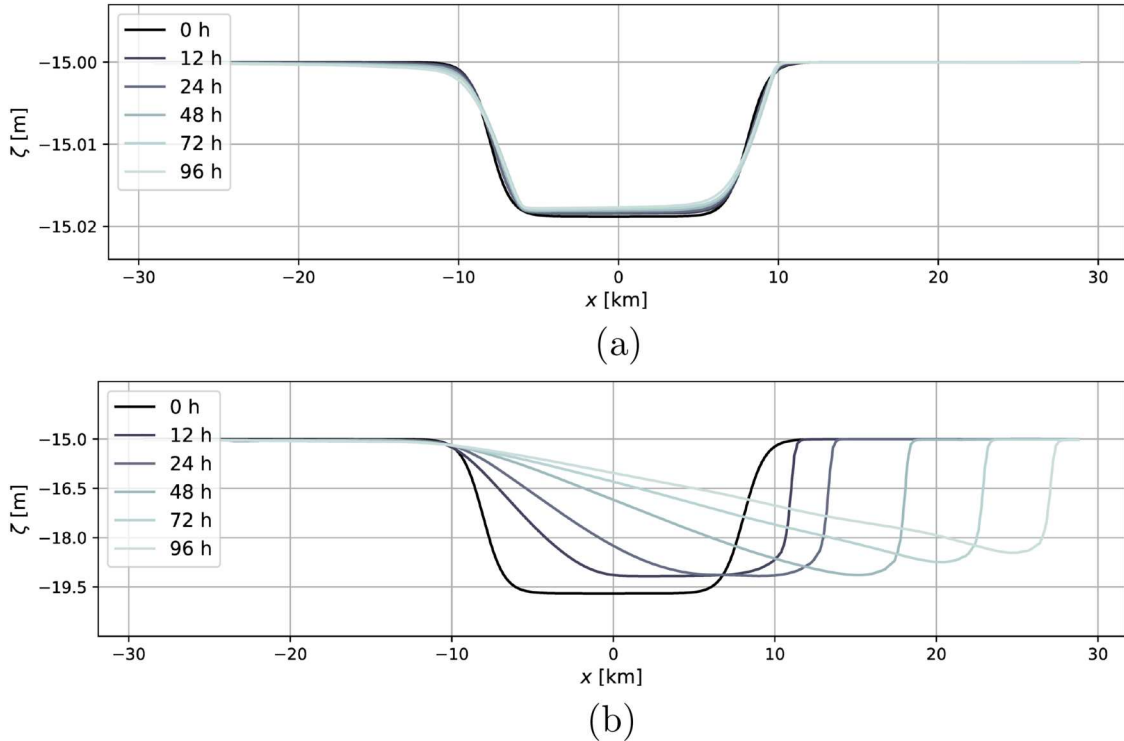


**Figure A2.** Simulated Kelvin waves along the boundary at  $y = 0$ , shifted along the  $x$ -axis according to the theoretic wave speed  $c$ . The darkest line shows the initial state of  $\zeta$  and the direction of motion is towards the right. (a) Small wave and (b) Big wave.

with the shape function

$$F(x) = 1.0 + \tanh\left(\frac{-\sqrt{(x - x_0)^2 + d_F}}{R/l_F}\right),$$

where  $(x_0, y_0) = (0, -200 \text{ m})$  is a reference point at the centre of the domain in  $x$  but outside of the southern boundary located at  $y = 0$ . Furthermore,  $d_F$  and  $l_F$  are shape parameters for the initial wave where we use the value 2.5 for both, and  $\zeta_0$  is a scaling. The constructed wave travels in  $x$ -direction along the wall at  $y = 0$ . The reduced gravity is set to  $g' = 0.01 \text{ m/s}^2$  and the equilibrium depth to  $H = -15 \text{ m}$ . The resulting phase speed becomes  $c \approx 0.39 \text{ m/s}$ , which is in big contrast to barotropic waves that typically have phase speeds in the range of  $10 - 100 \text{ m/s}$ .

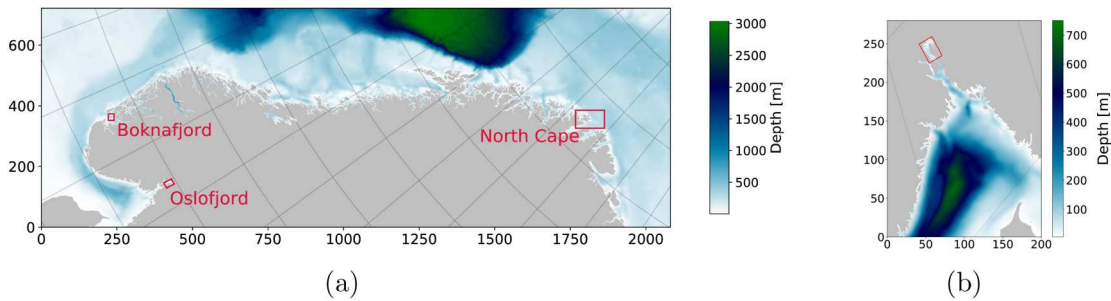
For a uniformly discretised domain with  $\Delta x = 200 \text{ m}$  and  $\Delta y = 400 \text{ m}$ , we run the numerical experiment for a small wave ( $\zeta_0 = 0.05$ ) and a big wave ( $\zeta_0 = 2.5$ ). Figure A2 shows the evolution of the two Kelvin waves, where we have shifted the solution along the  $x$ -axis according to the theoretical phase speed. For the small wave, we see that the Kelvin wave maintains the initial shape well and travels with the phase speed  $c$ . This is expected since the non-linear terms in the model become negligible for sufficiently small waves. With a

larger amplitude, the non-linearities become clearly visible in the solution, causing the shape of the Kelvin wave to deform towards a shock. This is also expected since the water depth is larger at the top of the wave than on the tail, causing the wave top to travel slightly faster. The wave is nevertheless maintained along the wall boundary, and hence demonstrates that Kelvin waves are well captured in the reduced-gravity model.

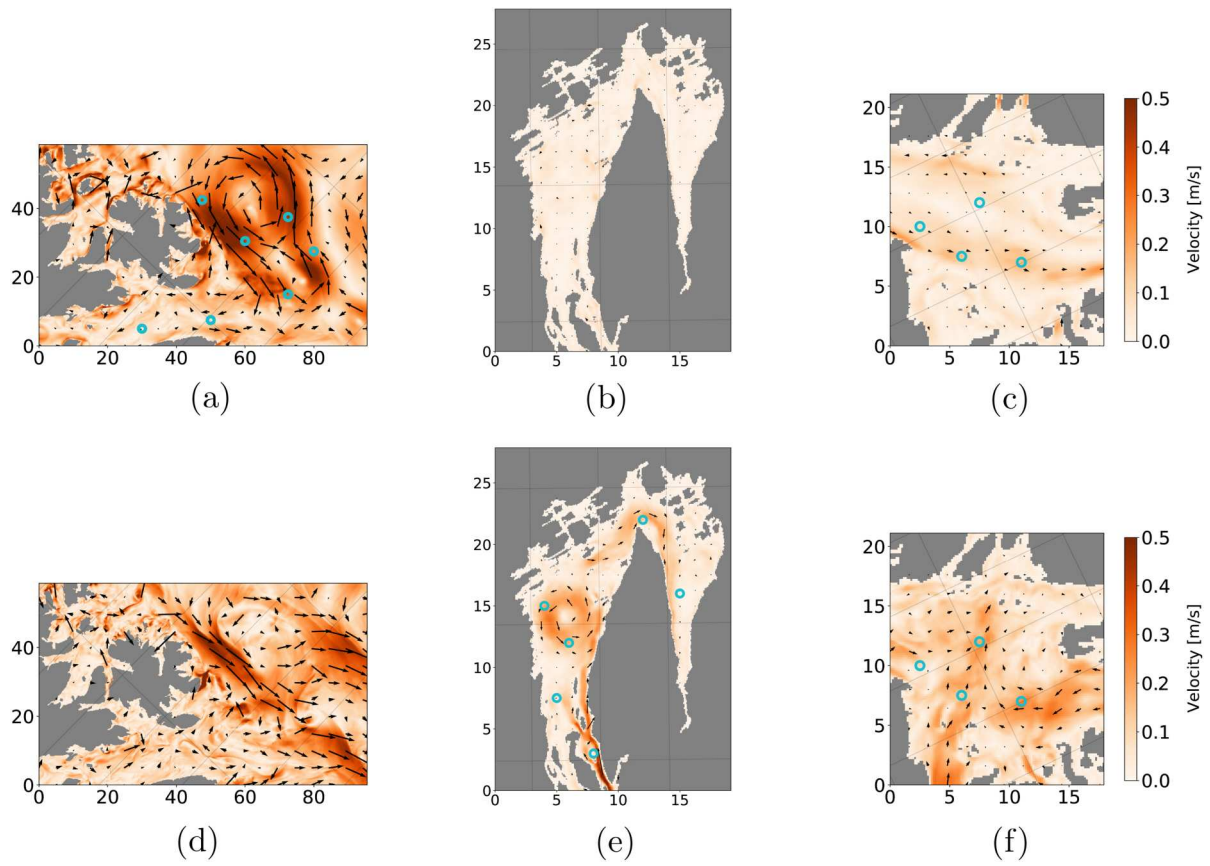
### Appendix 3. Details on initial conditions

Figure A3 explains the location of the cases considered in previous sections. For the Barents Sea, we use initial conditions from NorFjords at 2019-02-01 10:00. FjordOs provides initial fields for the Oslofjord at 2014-07-06 09:00:00. The Boknafjord simulation are initialised from NorFjords at 2019-11-01 11:00.

Figure A4 shows the reference initial conditions for all the three cases in Section 4. The barotropic currents at the North Cape are much stronger than in the other cases. In the Oslofjord, barotropic currents are remarkably small and usually much smaller than  $1 \text{ cm/s}$ . The baroclinic currents in the Oslofjord are significantly stronger in the strait east of Håøya, which is in accordance to the artificial scenario in Section 3.



**Figure A3.** The three cases from Section 4 marked on a map of Norway. (a) Areas of the three cases within the Norwegian coastal area and (b) Inner Oslofjord relative to Skagerrak.



**Figure A4.** Reference initial velocities for all cases and turquoise circles marking the initial drifter positions. The numbers along the axes represent km. (a) Barotropic velocities at North Cape, (b) Barotropic velocities in Oslofjord, (c) Barotropic velocities in Boknafjord, (d) Baroclinic velocities in 25 m-layer at North Cape, (e) Baroclinic velocities in Oslofjord and (f) Baroclinic velocities in Boknafjord.